Monthly Notices
of the
ROYAL ASTRONOMICAL SOCIETY

MNRAS **469,** 1573–1586 (2017)
Advance Access publication 2017 April 21

doi:10.1093/mnras/stx962

# Gas rotation, shocks and outflow within the inner 3 kpc of the radio galaxy 3C 33

Guilherme S. Couto,[1,2]★ Thaisa Storchi-Bergmann[2] and Allan Schnorr-Müller[2]

[1]*Departamento de Física-CFM, Universidade Federal de Santa Catarina, CP 476, 88040-900 Florianópolis, SC, Brazil*
[2]*Universidade Federal do Rio Grande do Sul, IF, CP 15051, 91501-970 Porto Alegre, RS, Brazil*

Accepted 2017 April 19. Received 2017 April 7; in original form 2017 February 9

## ABSTRACT

We present optical integral field spectroscopy – obtained with the Gemini Multi-Object Spectrograph – of the inner $4.0 \times 5.8\,\mathrm{kpc}^2$ of the narrow line radio galaxy 3C 33 at a spatial resolution of 0.58 kpc. The gas emission shows three brightest structures: a strong knot of nuclear emission and two other knots at ≈1.4 kpc south-west and north-east of the nucleus along the ionization axis. We detect two kinematic components in the emission lines profiles, with a 'broader component' (with velocity dispersion $\sigma \geq 150\,\mathrm{km\,s^{-1}}$) being dominant within an ∼1 kpc wide strip ('the nuclear strip') running from the south-east to the north-west, perpendicular to the radio jet, and a narrower component ($\sigma \leq 100\,\mathrm{km\,s^{-1}}$) dominating elsewhere. Centroid velocity maps reveal a rotation pattern with velocity amplitudes reaching $\sim\pm\,350\,\mathrm{km\,s^{-1}}$ in the region dominated by the narrow component, while residual blueshifts and redshifts relative to rotation are observed in the nuclear strip, where we also observe the highest values of the [N II]/H$\alpha$, [S II]/H$\alpha$ and [O I]/H$\alpha$ line ratios, and an increase of the gas temperature (∼18 000 K), velocity dispersion and electron density ($\sim 500\,\mathrm{cm^{-3}}$). We interpret these residuals and increased line ratios as due to a lateral expansion of the ambient gas in the nuclear strip due to shocks produced by the passage of the radio jet. The effect of this expansion in the surrounding medium is very small, as its estimated kinetic power represents only $2.6 \times 10^{-5} - 3.0 \times 10^{-5}$ of the AGN bolometric luminosity. A possible signature of inflow is revealed by an increase in the [O I]/H$\alpha$ ratio values and velocity dispersions in the shape of two spiral arms extending to 2.3 kpc north-east and south-west from the nucleus.

**Key words:** galaxies: active – galaxies: individual: 3C 33 – galaxies: jets – galaxies: kinematics and dynamics – galaxies: nuclei.

## 1 INTRODUCTION

The connection between active galactic nuclei (AGNs) and the host galaxy evolution has been a topic of debate in the past few decades with substantial evidence of a link between the two. The tight correlation between the masses of the central supermassive black holes powering the AGN and the properties of the bulges of the host galaxies (e.g. Greene & Ho 2006; Kormendy & Ho 2013) indicates that AGNs and their host galaxies coevolve in some manner, at least partially due to the feedback from the AGN. Theoretical studies indicate that the feedback from the AGN is a necessary ingredient in the evolution of galaxies, preventing them from becoming too massive (Di Matteo, Springel & Hernquist 2005; Wagner & Bicknell 2011; Fabian 2012). Radioactivity, in particular, influences the energetics and thermodynamics of the gas, generating gas ionization by shocks, aside from photoionization due to the AGN radiation (Best, Röttgering & Longair 2000; Fragile et al. 2004; Groves, Dopita & Sutherland 2004). Radio galaxies are interesting laboratories to study the effects of AGN feedback such as energy injection into the interstellar medium (ISM) and quenching of star formation.

Observational evidence of interaction between the AGN feedback and the ISM in radio galaxies has been claimed by several studies (Tremblay et al. 2009; Couto et al. 2013; Santoro et al. 2015; Roche et al. 2016). Integral Field Spectroscopy (IFS) provides a direct observation of the impact of the AGN on the ambient gas. IFS can also reveal possible feeding mechanisms of the AGN that promote gas inflow towards the nucleus. In this work, we present IFS study of the radio galaxy 3C 33.

3C 33 is a nearby ($z = 0.0597$, 1 arcsec corresponds to 1.15 kpc in the galaxy[1]) Fanaroff-Riley type II (FRII) radio galaxy, with its radio emission exhibiting two extended lobes and VLBI imaging showing two symmetric jets aligned with a large-scale structure,

★ E-mail: gcouto@if.ufrgs.br

[1] We adopt cosmological parameters $H_0 = 70.5\,\mathrm{km\,s^{-1}\ Mpc^{-1}}$, $\Omega_\Lambda = 0.73$ and $\Omega_M = 0.27$

which extend up to ∼120 kpc each (Leahy & Perley 1991; Giovannini et al. 2005). A high inclination angle of 75°–80° between the radio jet axis and the line of sight is indicated by the ratio between the fluxes of the jet and counterjet. The optical emission line spectrum of 3C 33 is typical of Seyfert 2 galaxies, with an [O III] luminosity of $L_{[O\,III]} \sim 1 \times 10^{42}$ erg s$^{-1}$. Tremblay et al. (2009), using *Hubble Space Telescope* Advanced Camera for Surveys (*HST*-ACS) data, showed that the [O III] and H$\alpha$+[N II] emission extends up to ∼2.5 kpc to the north-east and south-west from the nucleus in an 'integral sign' shape. Optical gaseous kinematic studies from Simkin (1979) and Heckman et al. (1985) indicate rotation around an axis approximately aligned with the radio jet axis (position angle PA∼20°).

This work presents a two-dimensional analysis of the kinematics and excitation of the gas within the inner ∼2 kpc of 3C 33. The paper is organized as follows. In Section 2 we describe the observations and the reduction of the data; in Section 3 we explain our emission line fitting strategy, along with the resulting gas excitation and kinematic maps we obtain from it; in Section 4 we discuss the results and present our interpretations to explain the physical processes taking place in 3C 33 circumnuclear region; and finally in Section 5 we present our conclusions.

## 2 OBSERVATIONS AND DATA REDUCTION

The observations were obtained with the Integral Field Unit of the Gemini Multi-Object Spectrograph (GMOS-IFU) at the Gemini North Telescope on 2010 August 17 (Gemini project GN-2010B-Q-66), in one-slit mode. Eight individual exposures of 3C 33 of 940 s were obtained, with a spectral coverage of 4500–7300 Å, centred at 5900 Å. The B600+_G5307 grating with the IFU-R mask was used. The GMOS-IFU, using one-slit mode, has a rectangular field of view (FoV) of ≈3.5 × 5 arcsec, corresponding to 4.0 kpc × 5.8 kpc at the galaxy. The spectral resolution is R ∼3800 at 7000 Å, derived from the full-width half-maximum (FWHM) of the CuAr emission lines. The seeing during the observations was 0.5 arcsec, as measured from the FWHM of a spatial profile of the calibration standard star. This corresponds to a spatial resolution of ≈580 pc at the galaxy.

The data reduction was accomplished using tasks in the GEMINI.GMOS IRAF package as well as generic IRAF[2] tasks. The reduction process comprised bias subtraction, flatfielding, trimming, wavelength calibration, sky subtraction, flux calibration, differential atmospheric dispersion, building of the data cubes at a sampling of 0.1 × 0.1arcsec, and finally combining the eight individual data cubes into a final data cube.

Bias subtraction from the science, flat and twilight raw frames was performed using the task GFREDUCE. Since the bias used in the reduction is not overscan subtracted, we did not apply overscan subtraction to the raw frames. Flat lamps were used to obtain the flat-field response map for each associated science frame also using GFREDUCE, in interactive mode. GSWAVELENGTH task was used to obtain the wavelength solution, using the arclamp exposures, applying a fifth-order Chevyshev polynomial to the profile. Since spectral dithering was performed in the observations, with half exposures being centred at 5850 Å and the other half at 5950 Å, we applied wavelength calibration to each set of data separately. RMS errors in the wavelength were typically ∼0.1 Å, which represents ∼20 per cent of spectral sampling of 0.46 Å per pixel. Flux calibration was performed using the GSCALIBRATE task, using a sensitivity function created from the standard star Feige 110, observed just prior to the flat and science exposures, which derived from the GSSTANDARD task. Finally, the cube creation for each science frame was performed using GFCUBE, where we also performed the atmospheric dispersion setting the keyword FL_ATMD on, and we combined the science cubes into a final cube using IMCOMBINE, correcting for offsets.

[2] IRAF is distributed by the National Optical Astronomy Observatory, which is operated by the Association of Universities for Research in Astronomy (AURA) under a cooperative agreement with the National Science Foundation.

## 3 RESULTS

Fig. 1 illustrates our IFU data and the FoV scale compared to other structures in 3C 33. In the top left panel we display a 1.4 GHz Very Large Array (VLA) radio image, originally published by Leahy & Perley (1991), with a beam size of 4 arcsec, covering a region of ≈250 × 200arcsec. We have tilted the VLA image to the same orientation of our GMOS data. The image shows two lobes from the radio jet extending roughly to the north and south from the nucleus, along a position angle (PA) of ≈− 19.5. Faint emission is observed between the two lobes, along with a hotspot in the galaxy core. The galaxy is displayed in the top central panel, in an image obtained with the GMOS acquisition camera (λ5620–6980, filter r_G0303), covering a region of 10 × 10 arcsec. Faint dark lanes are observed north from the nucleus, extending along the East–west direction, probably due to dust in a disc-like structure, suggesting that this is the near side of the galaxy. The top right-hand panel shows an *HST*-ACS narrow band image using the F551N ramp filter in the Wide Field Channel, with a central wavelength of λ5302, within a region of ≈3.5 × 5arcsec, which is the FoV of our GMOS-IFU data. This [O III] λ5007 rest-frame-centred image displays its peak emission in the nucleus (position N), with extended emission resembling spiral arms, where we identify positions A and B, from which we extracted sample spectra.

The bottom panels display the spectra extracted in the positions N (nucleus, adopted as the location of the continuum peak flux), A (located ≈1arcsec north-east from the nucleus) and B (located ≈0.6arcsec south-west from the nucleus) shown in the top right-hand panel, from the GMOS-IFU data cube. Each spectrum has a spatial aperture of 0.3arcsec radius, similar to our spatial resolution. We show in Fig. 1 the profiles of the main emission lines: H$\beta$λ4861, [O III] λλ4959, 5007, [N II] λλ6548, 84, Hαλ6564 and [S II] λλ6717, 31. The [O I] λλ6300, 34 emission lines are also strong, while He IIλ4686, H $\gamma$ λ4340 and [O III] λ4363 are weaker. The line profiles display strong red and blue wings at positions A and B, respectively. In fact, these wings are due to other kinematic components that will be discussed in further sections.

### 3.1 One-component fit with Gauss–Hermite polynomials

The gaseous centroid velocities, velocity dispersions and integrated fluxes were obtained by fitting Gauss–Hermite polynomials to the emission lines. The $h3$ and $h4$ Gauss–Hermite moments parametrize the deviations from a Gaussian profile, thus are good tracers of multiple emission-line components. $h3$ is related to the skewness of the profiles and $h4$ to its kurtosis. In other words, $h3$ measures asymmetric deviations from a Gaussian profile, such as blue or red wings, and $h4$ quantifies the peakiness of the profile, with $h4 > 0$ for a more peaked profile and $h4 < 0$ for a less peaked profile than a Gaussian curve. A Gaussian profile is obtained when $h3 = h4 = 0$.

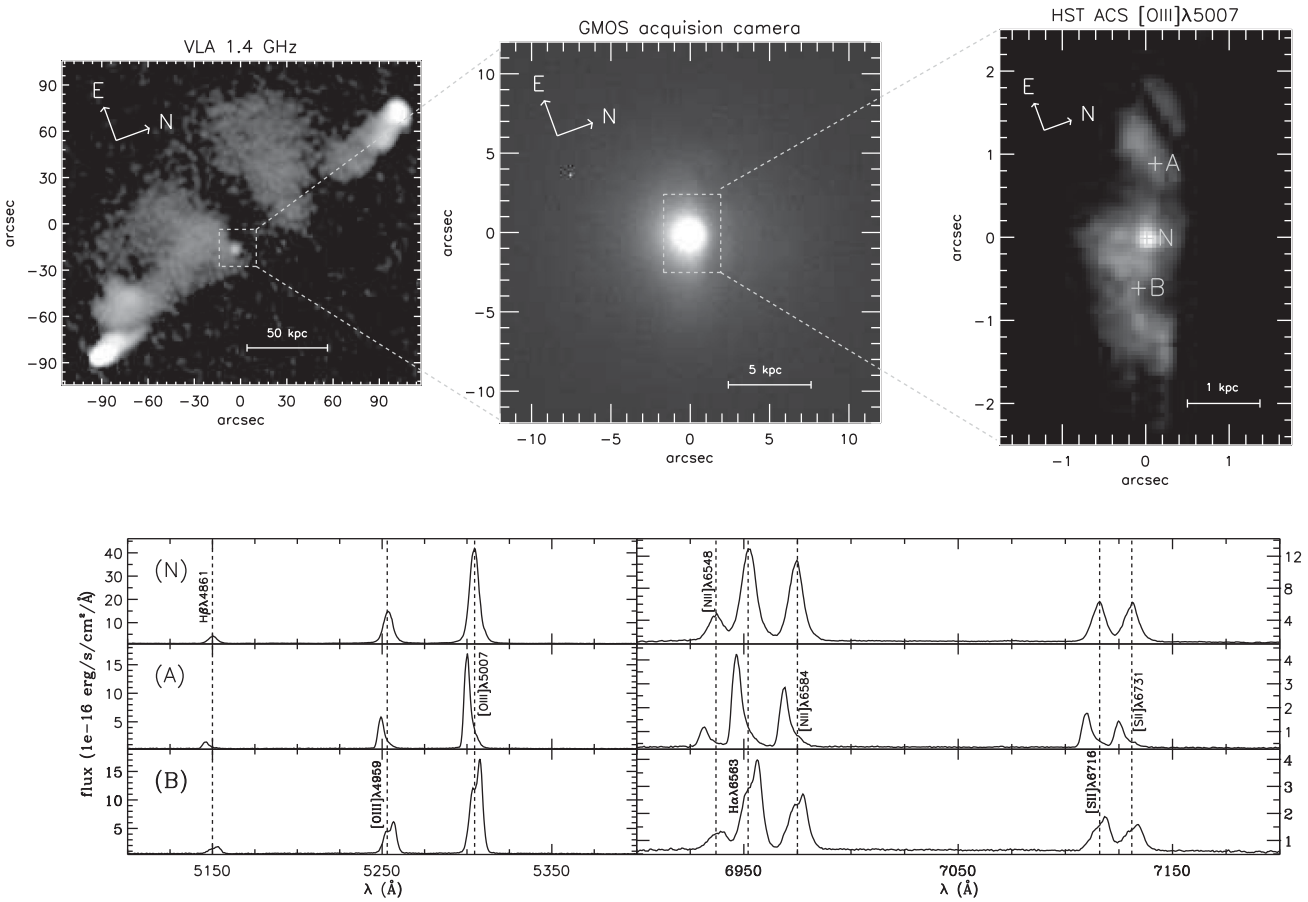


**Figure 1.** Top left-hand panel: 1.4 GHz VLA radio image of radio galaxy 3C 33 and its lobes. Top central panel: optical GMOS acquisition camera image of the galaxy. Top right-hand panel: *HST*-ACS [O III] λ5007 narrow band image within the FoV of the GMOS-IFU data. Bottom panels: Spectra extracted in positions N, A and B displayed in the top right panel.

In order to reduce the number of free parameters in the fit, the following physically motivated constraints were imposed:

(i) different lines from the same ionic species have the same kinematic parameters. For example, the [S II] λλ6717, 31 emission lines have the same centroid velocity and velocity dispersion. This was also done for the Gauss–Hermite parameters $h3$ and $h4$;

(ii) the [N II] λλ6548, 84 emission lines have the same centroid velocity and velocity dispersion as H$\alpha$;

(iii) the [N II] λ6548 flux was fixed as 1/3 of the [N II] λ6584 flux, in accordance with nebular physics (Osterbrock & Ferland 2006). This was also done for the [O III] λλ4959, 5007 and [O I] λλ6300, 34 emission lines.

In Fig. 2 we display the best Gauss–Hermite polynomial model fit to the [O III] λλ4959, 5007 emission lines, in the same positions marked in the top right-hand panel of Fig. 1. We also display the Gauss–Hermite parameters $h3$ and $h4$ for each position. Noticeably Gauss–Hermite polynomials are not a very good model for the emission-line profiles of some regions, such as positions A and B. However, for others, it does fit the profile nicely, like in position N. The distribution of the $h3$ and $h4$ values for the [O III] emission lines is shown in Fig. 3. Regions which present $|h3| > 0.03$ point to the presence of red (at locations mainly ≈ 1 arcsec east from the nucleus) and blue wings (at locations mainly ≈ 1 arcsec west from the nucleus). The $h4$ values reach high negative values in two narrow strips running approximately south-north, ≈ 1arcsec to the east and ≈ 1arcsec to the west of the nucleus, at the border of the regions with the highest positive and negative values of $h3$. Inspection of the profiles in these regions reveals that they actually present two kinematic components, like the spectrum of position B, to the west of the nucleus. We thus decided to also perform two-Gaussian fits to regions with $|h3|$ or $|h4|$ larger than 0.03. We discuss these fits further in the next subsection.

The measured integrated flux, centroid velocity and velocity dispersion maps for [O III] λ5007, H$\alpha$ and [S II] λ6717 emission lines, resulting from the Gauss–Hermite fits, are displayed in Fig. 4. Flux distributions are similar to that of the [O III]*HST* image, shown in the right-hand panel of Fig. 1. These flux distributions display, besides a strong emission peak at the nucleus, two other regions of enhanced emission to the north-east and south-west of the nucleus, at the locations of the spiral arms seen in the *HST* image. The centroid velocity maps display a pattern almost identical to the known 'spider' diagram, expected for rotation, with the kinematic major axis approximately aligned with the region of most extended emission in the flux maps. Blueshifts and redshifts are observed to the east and west of the nucleus, respectively, with high-velocity amplitudes ($\sim\pm$ 350 km s$^{-1}$). There is a noticeable distortion in the rotating pattern in the inner arcsecond or so, where we conclude there is a second kinematic component (see discussion below). This region also presents higher velocity dispersions $\sigma$ reaching $\sim$170 km s$^{-1}$. This region of highest $\sigma$ has the shape of a band $\sim$2 arcsec wide centred at the nucleus and running approximately perpendicularly to

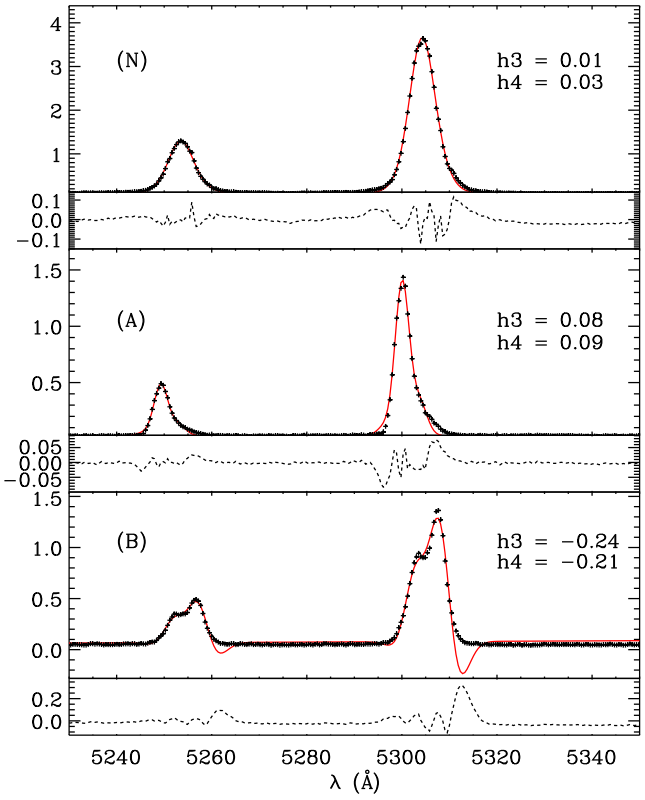


**Figure 2.** Fit of Gauss–Hermite polynomials to the [O III] λλ4959, 5007 emission-line profiles, for the three positions shown in the top right-hand panel of Fig. 1. Black crosses display spectrum data points and red lines represent the best model fitting to the profiles, with the resulting *h*3 and *h*4 parameters displayed in the upper right corner of each panel. Residuals are shown by dashed black lines. Flux units (*y*-axis) are $10^{-16}$ erg s$^{-1}$ cm$^{-2}$ Å$^{-1}$.

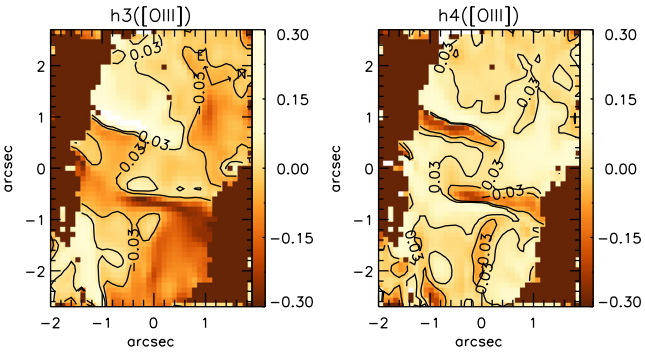


**Figure 3.** Gauss–Hermite *h3* and *h4* parameter maps, obtained from the fit of the [O III] λλ4959, 5007 emission lines.

the radio jet, represented by the blue line in Fig. 3. Hereafter, we will refer to this region as 'the nuclear strip'. Velocity dispersions are low outside these regions ($\sigma < 100\,\mathrm{km\,s^{-1}}$), with the lowest values of $<70\,\mathrm{km\,s^{-1}}$ displayed in the regions of highest centroid velocity amplitudes. Centroid velocities were obtained after the subtraction of the systemic velocity of $v_{\rm sys} = 17\,801.8\,\mathrm{km\,s^{-1}}$, resulting from the rotation model fitted to the H$\alpha$ velocity map, which we discuss further in Section 4.2. Also, we corrected the velocity dispersion values for the instrumental broadening ($\sigma_{\rm inst} = 44.3\,\mathrm{km\,s^{-1}}$).

Uncertainties in the Gauss–Hermite fits were estimated using Monte Carlo simulations of 100 iterations, in which Gaussian noise is added to the spectra. Expressing the flux uncertainty, $\epsilon_{\rm F}$, as a fraction of the integrated flux, $F$, we find that the main emission lines present $\epsilon_{\rm F}/F < 0.05$ throughout the whole FoV, except for the regions close to the borders of the data cube, where typical values of $\epsilon_{\rm F}/F \sim 0.1$, but can reach up to $\epsilon_{\rm F}/F \sim 0.3$ in weaker emission lines, like H$\beta$. The uncertainties of the centroid velocity and velocity dispersion measurements are similar, and display values of $\epsilon_v \sim \epsilon_\sigma < 10\,\mathrm{km\,s^{-1}}$ (but typically $\sim$2–3 km s$^{-1}$) in the nucleus and its surroundings. Close to the borders of the FoV, uncertainties in the velocity and velocity dispersions can reach $\sim$40 km s$^{-1}$. In Figs 3 and 4 (as in the other maps presented in this paper) we have masked out regions presenting uncertainty values higher than $\epsilon_{\rm F}/F = 0.1$, $\epsilon_v = 10\,\mathrm{km\,s^{-1}}$ or $\epsilon_\sigma = 10\,\mathrm{km\,s^{-1}}$.

Fig. 5 shows emission-line ratio maps obtained from the flux distributions. The highest values of [N II]/H$\alpha$, [S II]/H$\alpha$ and [O I]/H$\alpha$ (value ranges of 0.6–0.9, 0.7–0.85 and 0.25–0.35 for each of these three ratio distributions, respectively) are observed in the nucleus, and extended towards the nuclear strip, mainly in the former two ratio distributions. Intermediate values ($\sim$0.5, $\sim$0.5 and $\sim$0.2 for [N II]/H$\alpha$, [S II]/H$\alpha$ and [O I]/H$\alpha$, respectively) seem to extend towards the south-western border of our FoV. A counterpart of this extension is observed in the [O I]/H$\alpha$ ratio towards north-east from the nucleus, but not in [N II]/H$\alpha$ and [S II]/H$\alpha$. The lowest ratio values ($\sim$0.3, $\sim$0.35 and $\sim$0.15 for [N II]/H$\alpha$, [S II]/H$\alpha$ and [O I]/H$\alpha$ respectively) seem to be located in the regions of the highest velocity amplitudes, $\approx$1.5 arcsec east and west from the nucleus. The [O III]/H$\beta$ ratio is high throughout our FoV ([O III]/H$\beta$ > 10), due to the strong emission of the [O III] λ5007 line. The highest values ($\sim$14–16) are observed in the nucleus and extending in the same direction of the radio jet axis, indicated by the blue line in Fig. 5. Line ratio values then drop with distance from the nucleus until they reach the lowest values ($\sim$11) close to the borders of the FoV. The H$\alpha$/H$\beta$ ratio is high in the nucleus ($\sim$5.5), with highest values >6 observed towards the north-west. Values higher than H$\alpha$/H$\beta$ = 4 are observed north from the nucleus, extending along the East–west direction, following the dark lane observed in the acquisition camera image (top central panel of Fig. 1). Lower values of H$\alpha$/H$\beta \sim 3.5$ are observed south of the nucleus. Finally, the last ratio map displayed in Fig. 5, [S II]6717/31, shows the lowest values at the nucleus ($\sim$1) and somewhat higher ($\sim$1.2) in the nuclear strip. Higher ratios are observed outwards, reaching $\sim$1.5 at the borders of the FoV.

### 3.2 Two-components fit with Gaussian profiles

As mentioned in the previous section, for regions with |*h*3| or |*h*4| parameters (derived from the Gauss–Hermite polynomials fits) higher than 0.03, we performed a two-Gaussian fit in order to separate the two kinematic components of the emission lines. We used the same physical constraints used for the Gauss–Hermite fits, with an additional one: that the ratio between the two components should be the same for lines of the same ionic species, like [O III] λλ4959, 5007. Since the two components are very blended in some regions, such as at and around the nucleus, they become 'degenerate', and the fit is not well constrained. As the fits show that one component is broader than the other, we decided to identify the components as 'broad' and 'narrow' components. Examples of the fit of two components are shown in Fig. 6, for positions A and B. For regions with *h*3 and *h*4 close to 0, we have performed a single-Gaussian fit. We have then constructed separate flux and kinematic maps for the broad ($\sigma \geq 130\,\mathrm{km\,s^{-1}}$) and narrow ($\sigma < 130\,\mathrm{km\,s^{-1}}$) components.

We show in Fig. 7 the result of the two-Gaussian fits of the [O III] λ5007 profiles. We display the integrated flux, centroid velocity and

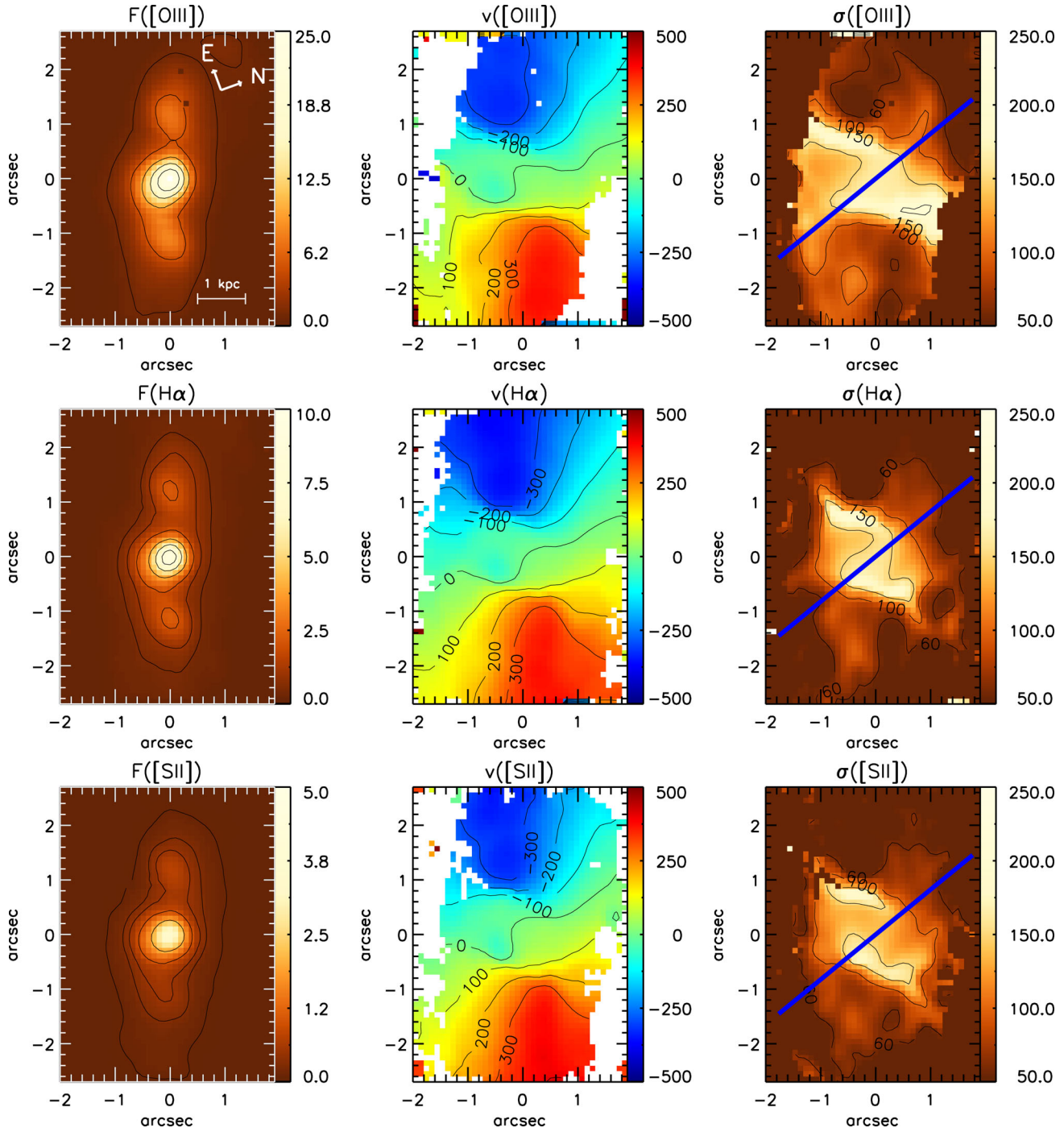


**Figure 4.** Line flux, centroid velocity and velocity dispersion distributions resulting from the Gauss–Hermite fit of the [O III] λ5007, H$\alpha$ and [S II] λ6717 emission lines. The blue line shows the orientation of the radio jet axis. Flux units are $10^{-16}$ erg s$^{-1}$ cm$^{-2}$ spaxel$^{-1}$. Centroid velocity and dispersion velocity units are km s$^{-1}$ .

velocity dispersion maps separately for the broad (top panels) and narrow (bottom panels) components. The flux distribution of the broad component is concentrated in the nucleus, with some extension towards the south-west and north-east within the nuclear strip. The emitting gas extending ∼12 arcsec south-west and north-east from the nucleus is traced by the narrow component. However, in other emission-line flux distributions, such as H$\alpha$, we derive more contribution of the narrow component close to the nucleus, but this is the result of the blending of the two components in this region.

The centroid velocity maps show that the rotation pattern is indeed traced by the narrow component, with the broader component presenting velocity values close to 0 km s$^{-1}$ without a clear pattern. Some redshifts are observed in the 'tail' structure of the broad component.

The $\sigma$ distributions show values of ∼90 km s$^{-1}$ along the north-east and south-west of the nucleus for the narrow component, and ∼170 km s$^{-1}$ for the broad component along the nuclear strip.

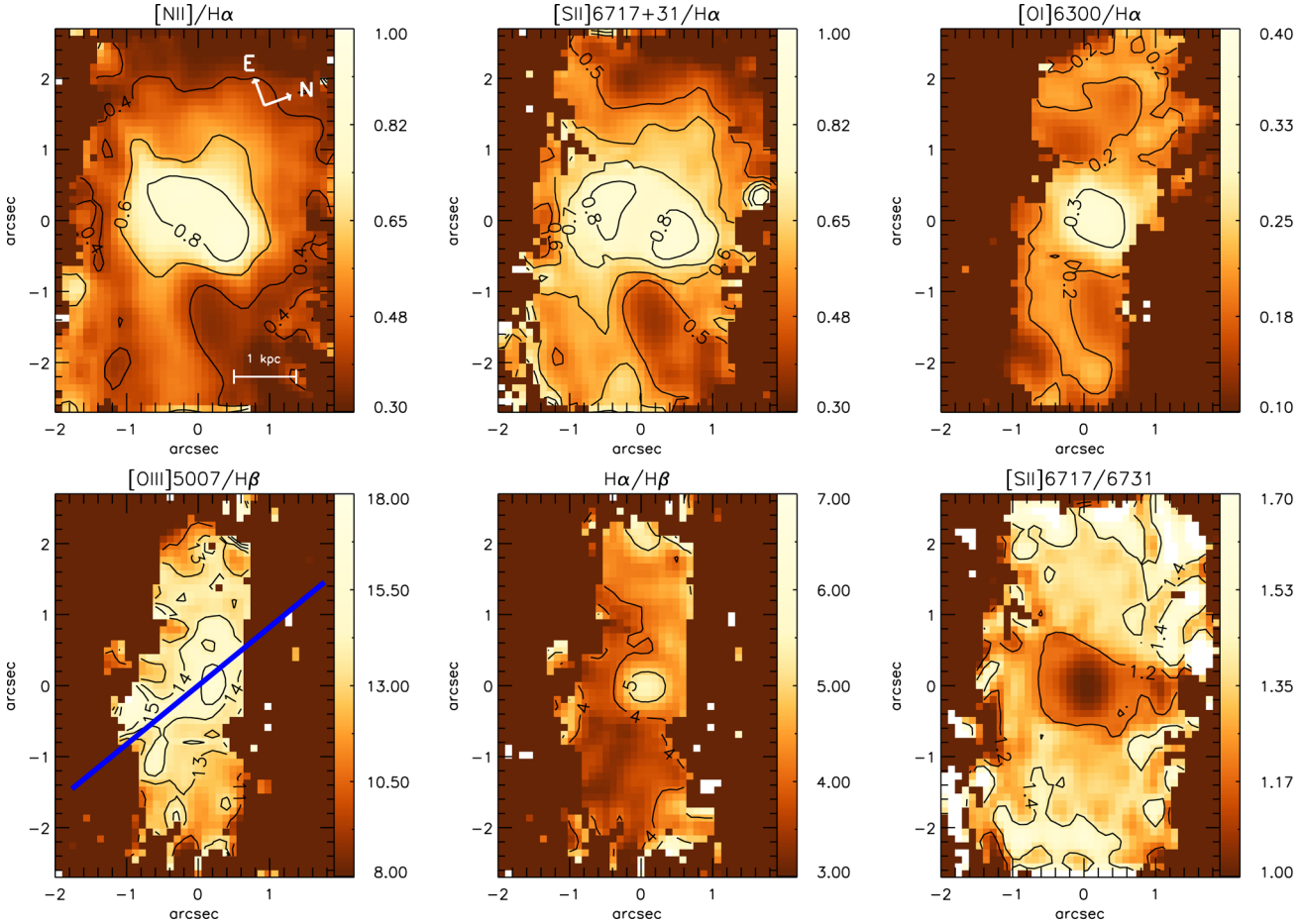


**Figure 5.** Line ratio maps, obtained from the flux distributions derived from the Gauss–Hermite fit. The blue line displays the radio jet axis.

### 3.3 Channel maps

Fig. 8 displays channel maps of the [O III] λ5007 emission-line profile. The maps were extracted in velocity bins of ≈55 km s$^{-1}$ along the emission line. The channel maps reveal two main components: a nuclear component, barely resolved within the inner 06 arcsec (∼700 pc), and an extra-nuclear extended component with blueshifted and redshifted velocities towards the north-east and south-west of the nucleus, respectively. The bulk of the extended emission has velocities of ±300 km s$^{-1}$, corresponding to the extended emitting gas observed ∼12 arcsec north-east and south-west of the nucleus in the flux maps. However, extended emission is also observed in higher velocity bins, up to ±450 km s$^{-1}$. At zero velocities (close to the systemic), we observe extended emission following the orientation of the radio jet.

## 4 DISCUSSION

### 4.1 Gas excitation

#### *4.1.1 Flux distributions*

The flux maps of the [O III] λ5007, Hα and [O I] λ6300 emission lines derived from the Gauss–Hermite fits (Fig. 4) show an elongated structure extending to ≈1.4 kpc north-east and south-west of the nucleus. In the two-Gaussian fits, this structure is traced by the narrow component (Fig. 7). This narrow component dominates in regions farther than ∼700 pc from the nucleus, while the broad component dominates within the inner ∼700 pc but extending along the nuclear strip running from the south-east to the north-west, but at lower intensity levels when compared to the narrow component.

#### *4.1.2 Line-ratio maps*

Emission-line ratios typical of Seyferts are observed over the whole FoV as shown in Fig. 5, in agreement with the strong [O III] λ5007 emission and high [O III]/Hβ line ratios, which places all covered locations of our FoV well into the Seyfert region of BPT diagrams (Baldwin, Phillips & Terlevich 1981; Kewley et al. 2006). The highest ratios of [N II]/Hα, [S II]/Hα and [O I]/Hα are observed along the nuclear strip. The increase in the latter line ratios can be attributed to the contribution of shocks (Allen et al. 2008). This hypothesis is supported by the fact that the radio jet runs approximately perpendicular to the nuclear strip. We propose a scenario in which the radio jet is causing a lateral expansion of the ambient gas as it travels outwards from the nucleus, forming the observed strip of increased line ratios approximately perpendicularly to the radio jet. In the case of [O I]/Hα, we also observe increased values up to 2.5 kpc to the north-east and south-west in the shape of two spiral arms that seem to correlate with those seen in the *HST* [O III] image in Fig. 1. A possible scenario is that this structure is tracing inflowing gas.

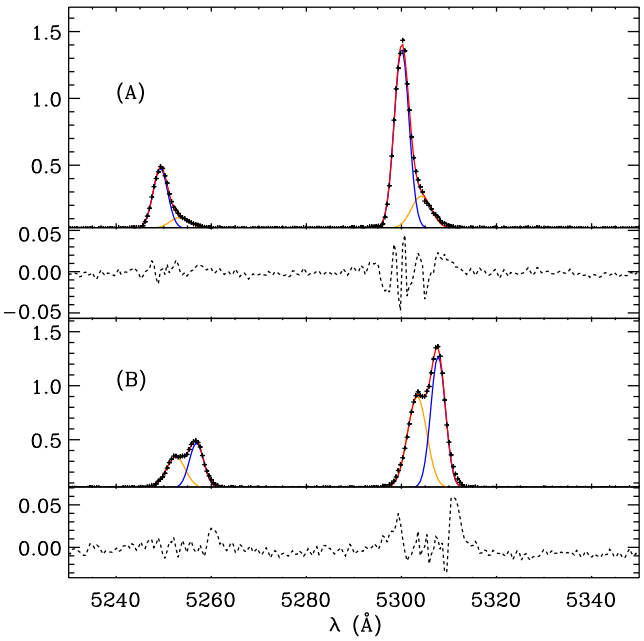


**Figure 6.** Two-Gaussian fit into the [O III] λλ4959, 5007 emission-line profiles, for positions A and B shown in the top right-hand panel of Fig. 1. Black crosses display spectrum data points and red lines represent the best model fitting to the profiles, with the narrow and broad component being represented by the blue and orange lines, respectively. Residuals are shown by dashed black lines. Flux units ($y$-axis) are $10^{-16}$ erg s$^{-1}$ cm$^{-2}$ Å$^{-1}$.

Along these arms, we also observe an increase in the velocity dispersion values (when compared to neighbouring regions) which is consistent with the presence of shocks in these spiral arms, allowing the gas to move inwards to feed the SMBH.

We have used the channel maps in the emission lines to also build line-ratio channel maps of [N II]/H$\alpha$ and [O III]/H$\beta$, which allow us to investigate the excitation according to the kinematics of the gas. These are shown in Figs 9 and 10. The highest [N II]/H$\alpha$ ratios are observed along the nuclear strip, most noticeable in the channels from $-84$ to $+106$ km s$^{-1}$, thus close to zero velocity. In these channels, the highest ratios are observed in blueshift to the west and in redshift to the east. On the other hand, the highest [O III]/H$\beta$ ratios are observed along the radio jet axis. The radio jet, which extends to far greater distances than probed by our FoV, may have 'cleared a path' in its way, pushing gas away in this direction and leading to an increased ionization parameter along this axis.

We observe high-ionizaton emission from [Fe X] λ6375, [Fe VII] λ5721 and [Fe VII] λ6087 at the nucleus with a suggested extension to the south. Higher signal-to-noise data would be necessary to confirm this extended emission, but if this is indeed the case, shock-driven outflows could be the responsible mechanism for the excitation, as previously observed in Seyfert galaxies (e.g. Rodríguez-Ardila et al. 2006), consistent with the scenario we propose where shocks are present near the nucleus.

#### *4.1.3 Electron density, O/H abundances, visual extinction and gas temperature*

The [S II] ratio map allows us to derive the electron density distribution (Osterbrock & Ferland 2006), which is shown in the upper left-hand panel of Fig. 11. The adopted temperature was 10 000 K. The highest density values ($>500$ cm$^{-3}$) are observed at the nucleus, with intermediate values of $\sim$200 cm$^{-3}$ along the nuclear strip, with lower values in the range 50–100 cm$^{-3}$ in the extended emission to the north-east and the south-west. This is in agreement with the scenario in which the nuclear strip is formed by the passage of the radio jet, due to compression of the surrounding gas, which is thus at least partially excited by shocks.

The upper right-hand panel of Fig. 11 shows the oxygen abundance (O/H) distribution for the emitting gas, derived from the relations of Storchi-Bergmann et al. (1998). As expected, the metallicity is higher in the nucleus, with values of $12 + \log(\mathrm{O/H}) \sim 8.7$. A slightly higher metallicity is observed ≈0.3arcsec north-west from the nucleus. Although 3C 33 shows metallicity values typical of AGNs, these values are somewhat lower than those observed for Seyfert galaxies (typically 8.9–9.3), and is actually comparable to values displayed by low-ionization nuclear emission-line region (Storchi-Bergmann et al. 1998). This suggests that the origin of a part of the ionized gas may be the capture of a gas rich, lower metallicity galaxy, as is probably the case of another known radio galaxy, Pictor A, for which we performed a similar study in Couto et al. (2016).

The H$\alpha$/H$\beta$ ratio map of Fig. 5 was used to obtain the visual extinction $A_V$ map. We adopted the reddening law from Cardelli, Clayton & Mathis (1989), and assuming case B recombination (Osterbrock & Ferland 2006) we obtain

$$A_V = R_V\, E(B-V) = 6.9 \times \log\left(\frac{\mathrm{H}\alpha/\mathrm{H}\beta}{3.1}\right). \quad (1)$$

The corresponding visual extinction map is shown in the bottom left-hand panel of Fig. 11. The highest values (∼1.5 mag) are observed at the nucleus, while values of ∼1 mag are observed ∼1 − 2arcsec north-west of the nucleus, in the region where a faint dark lane is observed in the optical continuum acquisition image (see the top central panel of Fig. 1). We propose that this lane is located along an inclined disc that we observe in rotation in the gas velocity map, as discussed below.

Finally, the bottom right-hand panel of Fig. 11 displays the temperature of the gas, as derived from the [O III] λ4959+5007/4363 ratio. We also used the [S II] ratio map as an input parameter in the PYNEB code (Luridiana, Morisset & Shaw 2015), to derive the temperature map (which is shown in units of $\times$ 10$^3$ K). Although the coverage of the region where we could measure the temperature is more limited than other line ratio maps, we find the highest temperatures of about ∼18 000 K along the nuclear strip, in particular in the regions where we observe the highest velocity dispersion values. The fact that the temperature increases outwards from the nucleus to drop again at farther distances indicates that the dominant mechanism responsible for this increase is not photoionization by the AGN, but shocks. This is also supported by the higher velocity dispersion and line ratios values (e.g. [N II]/H$\alpha$), as we previously pointed out. In the following section, we discuss further evidence for the presence of shocks.

### 4.2 Gas rotation

Centroid velocity maps of the ionized gas display a typical rotation pattern, which is traced both by the Gauss–Hermite fit in Fig. 4 and by the narrow-component Gaussian fit in Fig. 6. We fitted a kinematic model of circular orbits in a plane (van der Kruit & Allen 1978; Bertola et al. 1991) to the H$\alpha$ centroid velocity field derived from the Gauss–Hermite fit. The model is described by the

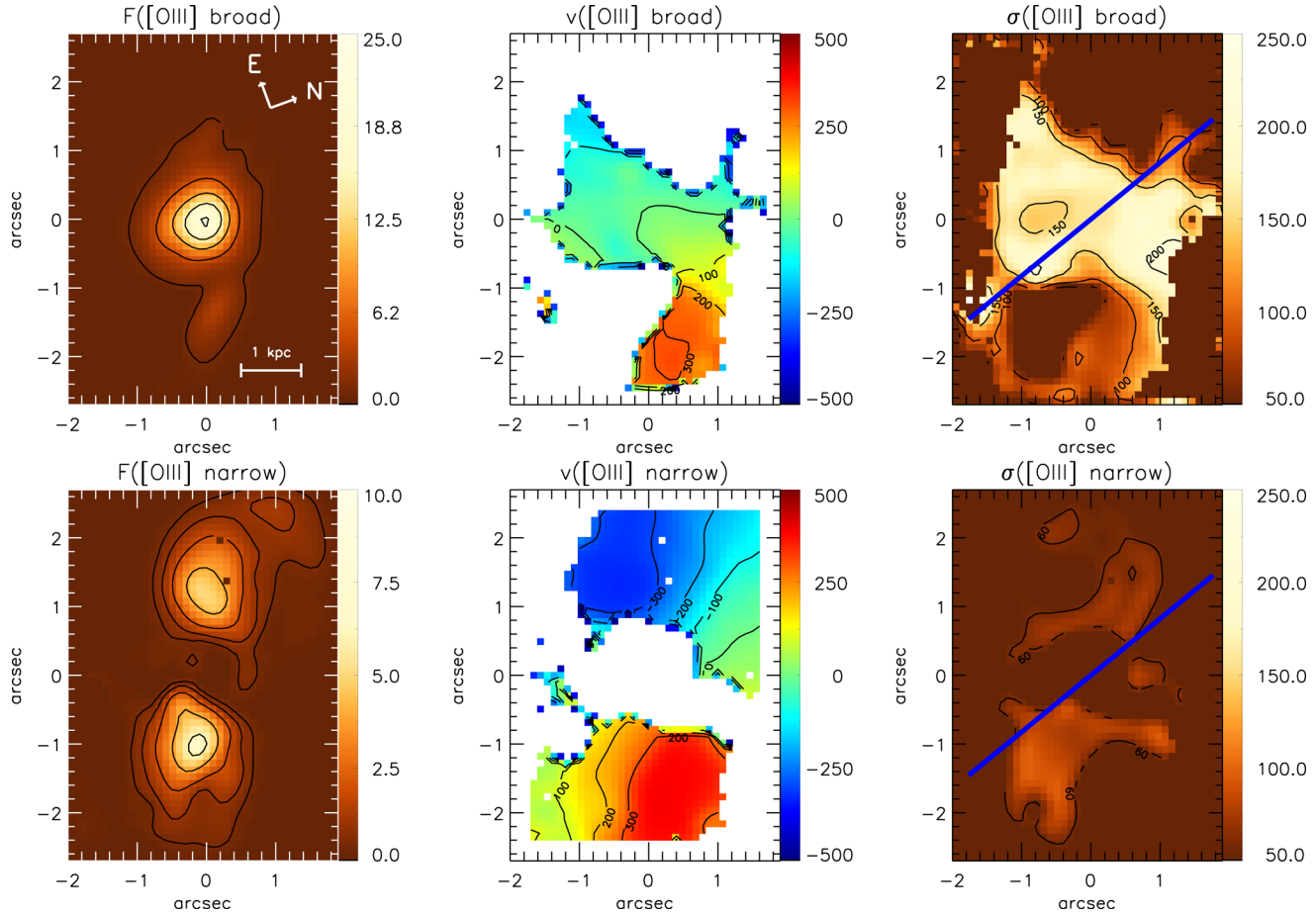


**Figure 7.** Integrated flux, centroid velocity and velocity dispersion distributions resulted from the two- Gaussian fit of the [O III] λ5007 line, for the broad and narrow component. The blue line displays the radio jet axis. Flux units are $10^{-16}$ erg s$^{-1}$ cm$^{-2}$ spaxel$^{-1}$. Centroid velocity and dispersion velocity units are km s$^{-1}$ .

equation:

$$v_{\rm mod}(R,\Psi) = v_{\rm sys} + \frac{A\,R\cos(\Psi-\Psi_0)\sin\theta\cos^p\theta}{\{R^2[\sin^2(\Psi-\Psi_0)+\cos^2\theta\cos^2(\Psi-\Psi_0)]+c_0^2\cos^2\theta\}^{p/2}}, \quad (2)$$

where $v_{\rm sys}$ is the systemic velocity, $A$ is the centroid velocity amplitude, $r$ and $\Psi$ are the radial and angular coordinates of a given pixel in the plane of the sky, $\Psi_0$ is the position angle of the line of nodes, $c_0$ is a concentration parameter (constraining the radius at which the centroid velocity reaches 70 per cent of the amplitude $A$) and $\theta$ is the disc inclination ($\theta = 0$ for a face-on disc). Finally, the parameter $p$ measures the slope of the rotation curve after reaching the maximum amplitude. This parameter was fixed at $p = 1$, which corresponds to an asymptotically flat rotation curve at large radii. The model also returns the centre of rotation $(x_0, y_0)$ in terms of the distance to a reference pixel, which in our case we consider to be the peak of the continuum.

We used a Levenberg–Marquardt least-squares algorithm to obtain the best-fitting model shown in Fig. 12. The resulting parameters from the fit are displayed in Table 1. Uncertainties are smaller than 5 per cent for all parameters.

The rotation model velocity map (central panel of Fig. 12) is a very good representation of the H$\alpha$ velocity field, confirming that it is dominated by rotation. The residuals, shown in the right-hand panel of Fig. 12, are small and very close to zero, except for two regions with residuals of ∼100 km s$^{-1}$ , one ∼0.5arcsec east from the nucleus showing redshifts and another ∼0.5arcsec west showing blueshifts. These residuals are in agreement with the scenario we propose in which this region is tracing a lateral expansion of the gas, pushed away by the radio jet. We also note that these regions are where we observe the highest [N II]/H$\alpha$ values in the channel maps of Fig. 9. As the near side of the galaxy is probably the north/northwest, where we observe the dust lane, a possible interpretation for the above residuals is the result of the lateral expansion of the gas by the shock produced by the ratio jet, with blueshifted residuals in the near side of the disc and redshifts in the far side of the disc. Another region, located ∼1.2arcsec east from the nucleus, presents substantial residual values of ∼− 50 km s$^{-1}$ . However, we note that these residuals are an artificial feature generated from the higher residuals located close to it, along the nuclear strip. We re-fitted the rotation model to the velocity map, masking out the nuclear strip, and obtained residuals close to zero in this region.

The best-fitting rotating disc parameters give an inclination of $\theta = 66°$, with velocity amplitude of $A = 453.7$ km s$^{-1}$ . This amplitude is very high for rotating discs originated from secular motions within the galaxy,[3] and suggests that the rotating gas was recently acquired via an interaction, a process quite common in radio

[3] See e.g. Sofue et al. (1999), where the authors found that spiral galaxies usually present rotating velocities of 200–250 km s$^{-1}$ at ∼2 kpc radius.

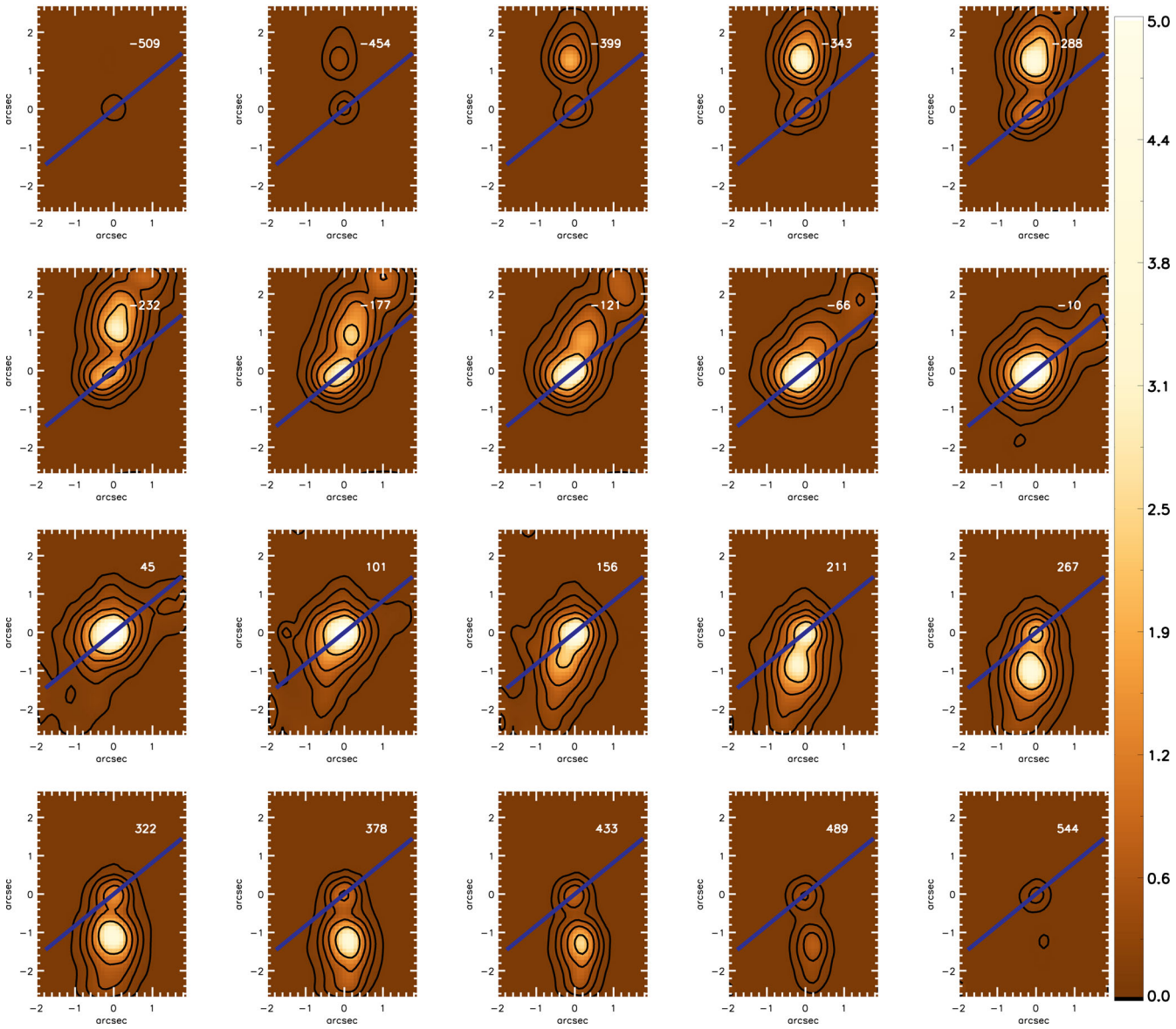


**Figure 8.** Channel maps along the [O III] λ5007 emission-line profile, in order of increasing velocities shown in the top of each panel in units of km s$^{-1}$ . Flux units are $10^{-16}$ erg s$^{-1}$ cm$^{-2}$ spaxel$^{-1}$. The green dashed line displays the radio jet axis.

galaxies (Ramos Almeida et al. 2011). The orientation of the line of nodes, $\Psi_0 = 83\overset{\circ}{.}3$, is tilted by $\sim 10^\circ$ relative to the ionization axis (PA $\sim 70^\circ$). This means that the ionization cone, whose axis probably coincides with that of the radio jet, is intercepting a narrow patch of the disc. This is supported by the [O III] channel maps (Fig. 8) that show that the bulk of the emission is not observed at the highest velocities (along the major axis, where velocities of up to $\sim \pm$ 400 km s$^{-1}$ are observed) but at velocities $\sim \pm$ 300 km s$^{-1}$ .

### 4.3 The nuclear strip

Fig. 13 illustrates the signature of shocks in the gaseous kinematics, in particular, along the nuclear strip. The upper panels display the gas velocity dispersion, the residuals between the gas velocities and the rotation model and the gas temperature side by side to show that the residuals are highest ($> \pm$50 km s$^{-1}$ ) in the regions where the velocity dispersion values are also the highest ($>$150 km s$^{-1}$ ), accompanied with an increase of the temperature that reaches $\sim$18 000 K in these regions. In the bottom panels we display the relation between the H$\alpha$ velocity dispersion and both the H$\alpha$ centroid velocity and model residuals, for each pixel of the GMOS FoV. In the $\sigma_{\mathrm{H}\alpha}$ versus $v_{\mathrm{H}\alpha}$ diagram, we can distinguish two main kinematical regimes: (1) pixels tracing the rotation present low-velocity dispersion ($\sim$50 km s$^{-1}$ ) and are found closer to the $v = 4\sigma$ line; (2) pixels tracing the shocked and expanding gas along the nuclear strip present higher velocity dispersion ($>$100 km s$^{-1}$ ) and are found closer to the $v = \sigma$ relation. In the $\sigma_{\mathrm{H}\alpha}$ versus residuals diagram, pixels with low-velocity dispersion have velocity residuals close to zero, while pixels with high-velocity dispersion have higher velocity residuals. These diagrams present strong evidence of outflowing gas in the two regions of enhanced velocity dispersion. Added with the observed increase of the line ratios, electronic density and gas temperature, they support our interpretation that the outflow is producing shock ionization of the gas.

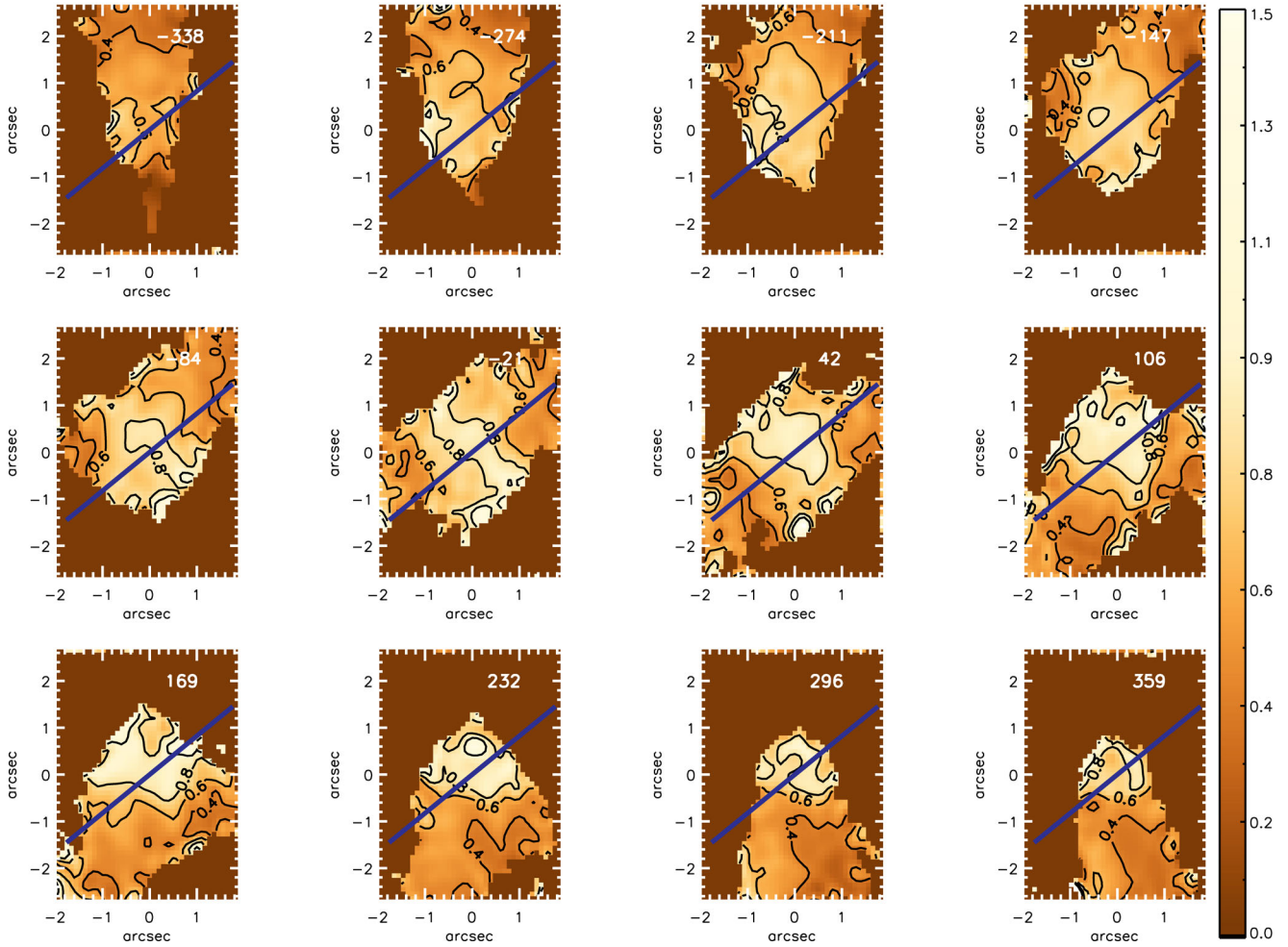


**Figure 9.** Channel maps of the [N II]/H$\alpha$ emission-line ratio, in order of increasing velocities shown in the top of each panel in units of km s$^{-1}$ . Velocity bins are averages of the [N II] and H$\alpha$ channels. The blue line displays the radio jet axis.

### *4.3.1 Mass outflow rate and outflow kinetic power*

In this section, we estimate the mass outflow rate related to the nuclear strip. Analysing the outflow shape in the residuals distribution as seen in Fig. 13, we assume that the outflow is located along an inner radius of the rotating disc, in a section of it. We thus assume a cylindrical geometry, with disc-like dimensions, with a base radius extending up to the edge of the observed residual centred at the nucleus, $r = 0.8$arcsec, and a small height of $h = 0.2$arcsec. The mass flowing through the cross-section of the assumed geometry is obtained from:

$$\dot{M}_{\rm out} = n_{\rm e}\, m_{\rm p}\, v_{\rm out}\, A\, f\,, \qquad (3)$$

where $m_{\rm p} = 1.7 \times 10^{-24}$ g is the proton mass, $n_{\rm e}$ is the electron density, $v_{\rm out}$ is the velocity of the outflow perpendicular to $A = 2\pi\, r\, h = 1.3 \times 10^{43}$ cm$^2$, which is the cross-section of the disc edge and $f$ is the filling factor.

The volume of the assumed geometry is $V = 1.8 \times 10^{64}$ cm$^3$, and the mean electron density and the H$\alpha$ luminosity in the nuclear strip are $\approx$300 cm$^{-3}$ and $2.6 \times 10^{41}$ erg s$^{-1}$, respectively, which results in $f = 1.3 \times 10^{-4}$ (see Peterson 1997 for details). Assuming the outflow velocity to be the highest velocity observed in the residuals, $v_{\rm out} = 118$ km s$^{-1}$, we obtain from equation (3) $\dot{M}_{\rm out} = 0.15\,{\rm M}_\odot$ yr$^{-1}$. However, we are probably underestimating the outflow velocity, since it must have a projection angle with the line of sight. We may assume that the bulk of the outflowing gas is located along the rotating disc modelled in Section 4.2. Thus, correcting the outflow velocity by a projected angle of 24.°3, we obtain that $v_{\rm out} = 129$ km s$^{-1}$, resulting in an outflow mass rate of $\dot{M}_{\rm out} = 0.17\,{\rm M}_\odot$ yr$^{-1}$.

We now use these estimations to calculate the outflow kinetic power (Holt et al. 2006), as

$$\dot{E} \approx \frac{\dot{M}_{\rm out}}{2}\left(v_{\rm out}^2 + 3\sigma^2\right), \qquad (4)$$

with the mean H$\alpha$ velocity dispersion $\sigma = 166$ km s$^{-1}$ at the nuclear strip. Using both the observed and projected outflow velocities, we obtain a range $4.7 < \dot{E} < 5.3 \times 10^{39}$ erg s$^{-1}$.

We can also compare these values with the AGN bolometric luminosity. We estimate that $L_{\rm bol} \approx 100 \times L({\rm H}\alpha)$, where $L({\rm H}\alpha)$ is the total observed H$\alpha$ luminosity, as we calculate in Section 4.4. We estimate that the AGN bolometric luminosity for 3C 33 is $L_{\rm bol} = 1.7 \times 10^{44}$ erg s$^{-1}$, implying that the outflow kinetic power is only $2.6 < \dot{E}/L_{\rm bol} < 3.0 \times 10^{-3}$ per cent. These values are comparable to estimates of outflow kinetic power of ionized gas in other local radio galaxies, such as Arp 102B and 3C 293 (Couto et al. 2013; Mahony et al. 2016). However, the bulk of outflowing gas mass in these objects is usually found in neutral and molecular phases (i.e. Feruglio et al. 2010; Nesvadba et al. 2010;

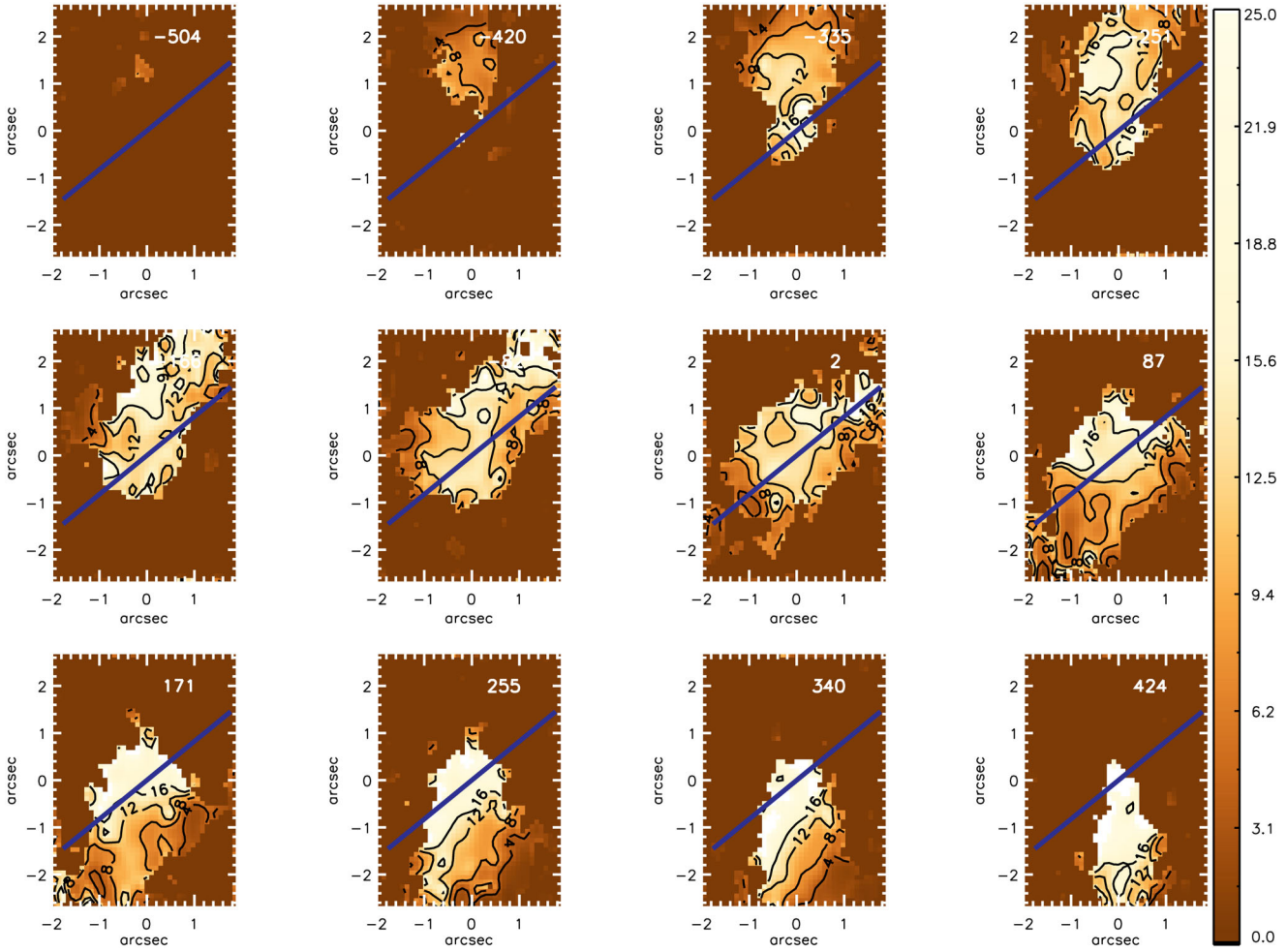


**Figure 10.** Channel maps of the [O III]/H$\beta$ emission-line ratio, in order of increasing velocities shown in the top of each panel in units of km s$^{-1}$. Velocity bins are averages of the [O III] and H$\beta$ channels. The blue line displays the radio jet axis.

García-Burillo et al. 2014), and this is probably the case also for 3C 33. In these phases, mass outflow rates are up to two to three orders of magnitude higher than for ionized gas. Also, we note that, considering this is an FRII radio galaxy presenting a large-scale jet, most of the feedback probably occurs in the surrounding intergalactic medium.

### 4.4 Emitting gas mass

We can estimate the mass of the ionized gas as (Peterson 1997):

$$M \approx 2.3 \times 10^5 \, \frac{L_{41}(\mathrm{H}\,\alpha)}{n_3^2} \, \mathrm{M}_\odot \, , \qquad (5)$$

where $L_{41}(\mathrm{H}\,\alpha)$ is the H$\alpha$ luminosity in units of $10^{41}$ erg s$^{-1}$ and $n_3$ is the electron density in units of $10^3$ cm$^{-3}$.

We corrected the total H$\alpha$ luminosity for reddening, assuming $R_V = 3.1$ from Cardelli et al. (1989), resulting in $L(\mathrm{H}\,\alpha) = 4\pi \mathrm{d}^2 \, F(\mathrm{H}\,\alpha) \, 10^{C(\mathrm{H}\,\alpha)} = 1.7 \pm 0.1 \times 10^{42}$ erg s$^{-1}$. Using the electron density map shown in Fig. 11, we could map the ionized gas mass distribution over our FoV, as shown in Fig. 14. The total ionized gas mass within the inner ∼2.5 kpc radius results in $M = 4.1 \pm 1.7 \times 10^8$ M$_\odot$. This mass is consistent with the values obtained in previous studies of other radio galaxies, such as that of Tadhunter et al. (2014), who estimate that strong-line radio galaxies (like 3C 33) with redshifts between 0.05 and 0.7 have gas masses of $1.0 \times 10^8 < M < 3.7 \times 10^{10}$ M$_\odot$, with a median of $1.2 \times 10^9$ M$_\odot$.

## 5 CONCLUSIONS

We have measured the gaseous kinematics and excitation in the inner 4.0 × 5.8 kpc of the narrow line radio galaxy 3C 33, from optical spectra obtained with the GMOS integral field spectrograph on the Gemini North telescope, at a spatial resolution of ≈580 pc at the galaxy.

We observe elongated gas emission extending to ≈2 kpc north-east and south-west of the nucleus, a direction that we identify as that of the ionization axis. We could separate two kinematical components in the GMOS FoV: a broader component, with velocity dispersions of $\sigma \geq 150$ km s$^{-1}$, which is dominant within a 1 kpc wide 'nuclear strip' – running from the south-east to the north-west, approximately perpendicular to the direction of the radio jet – and a narrower component, with velocity dispersions of $\sigma \leq 100$ km s$^{-1}$, which dominates the emission beyond the nuclear strip.

The narrow component traces the rotation pattern of the gas, observed in the centroid velocity maps. We obtain a good fit when modelling the H$\alpha$ velocity field with a rotation model with a velocity amplitude of ∼450 km s$^{-1}$ and an angle between the disc plane and the plane of the sky of ∼65°. Residual blueshifts and redshifts

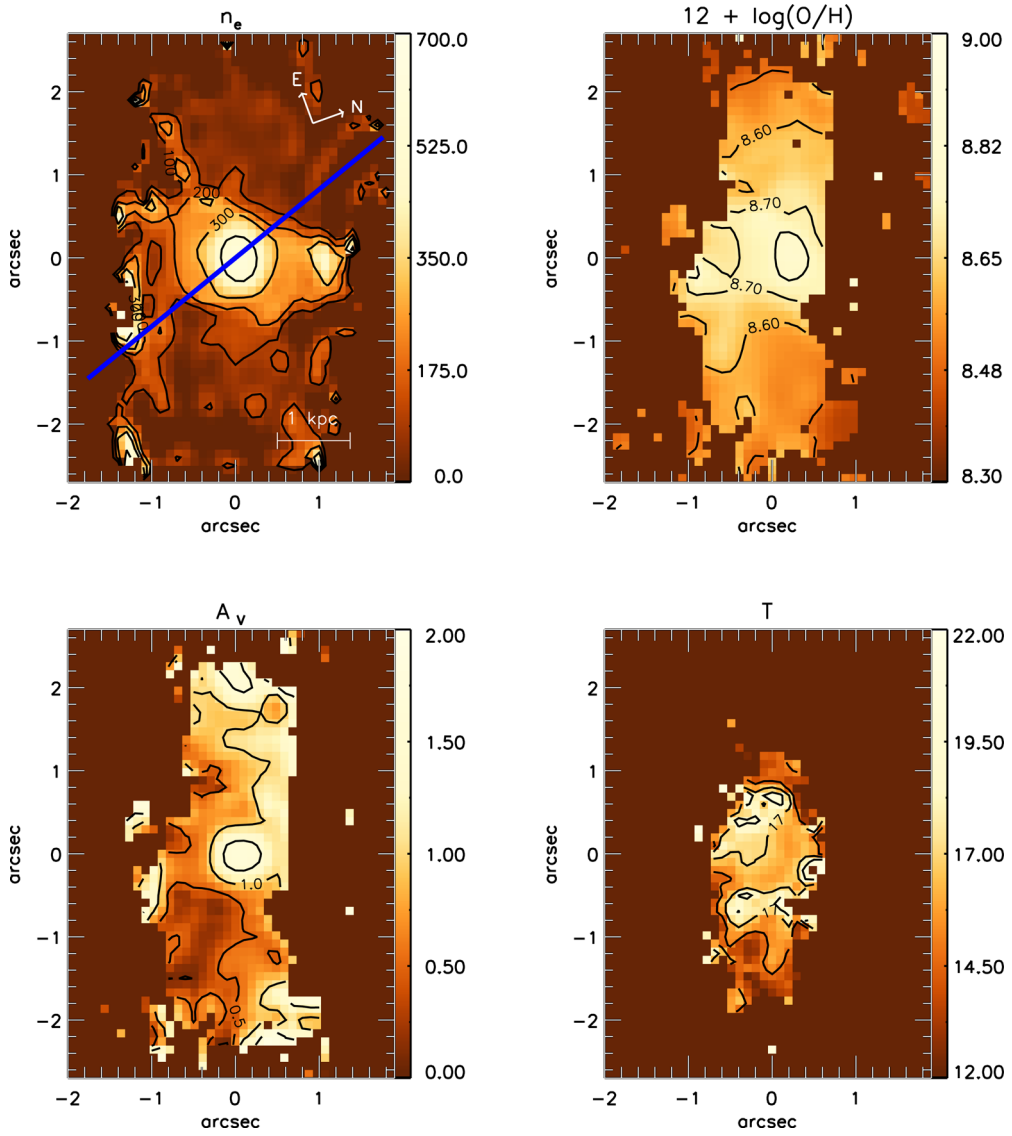


**Figure 11.** From upper left to bottom right: electron density, oxygen abundance, visual extinction distribution maps and gas temperature. Density units are $cm^{-3}$, $A(V)$ is in magnitudes and temperature is in $\times\ 10^3$ K. The blue line displays the radio jet axis.

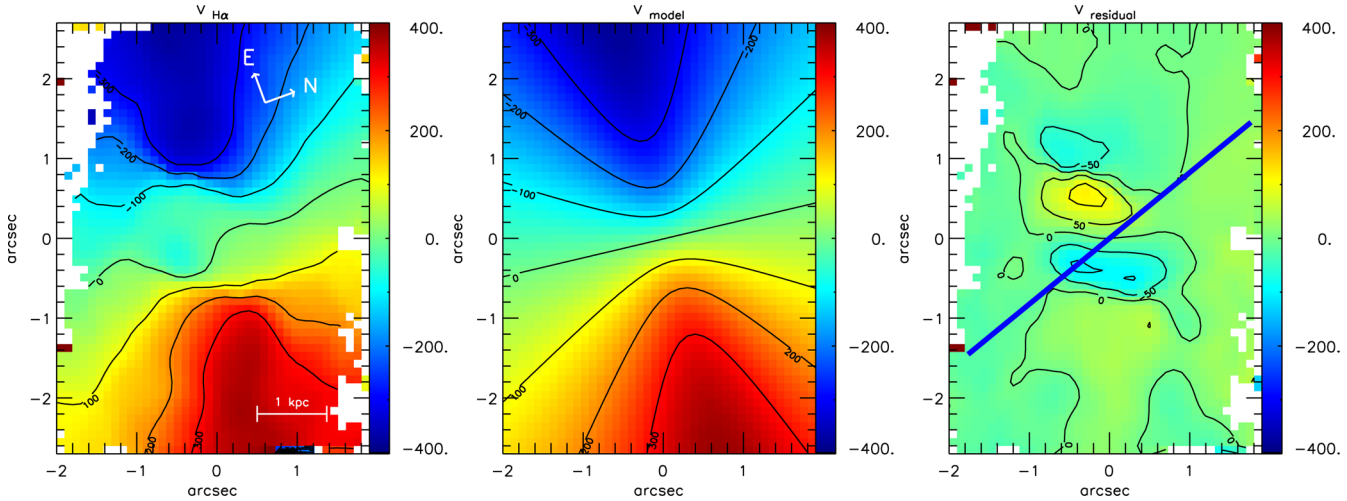


**Figure 12.** Gaseous rotating disc model for H$\alpha$ emission line. Left: H$\alpha$ velocity map obtained from the Gauss–Hermite fit. Central: model of the rotation curve. Right: residual map. The blue line displays the radio jet axis.

**Table 1.** Best-fitting parameters from the disc kinematic model.

| | |
|---|---|
| $\Psi_0$ (deg) | 83.3 |
| $\theta$ (deg) | 65.7 |
| $c_0$ (arcsec) | 1.2 |
| $A$ (km s$^{-1}$) | 453.7 |
| $v_{sys}$ (km s$^{-1}$) | 17 801.8 |
| $x_0$ (arcsec) | 0.06 |
| $y_0$ (arcsec) | 0.01 |
| $p$ [fixed] | 1 |

of $\sim$100 km s$^{-1}$ are observed within the nuclear strip. Rotation is also observed in the channel maps of the [O III] $\lambda$5007 emission line, in which we observe that the bulk of emission is located in velocity bins close to $\sim$300 km s$^{-1}$, corresponding to the orientation of the ionization axis, while the emission at higher velocity bins – and lower intensities – are shifted to a higher position angle, in agreement with the orientation of the line of nodes of the disc model (65°). Regions of highest emission are also extended along the radio jet axis in the velocity channels close to zero (in the galaxy velocity frame).

The nuclear strip is characterized by high-velocity dispersions ($\sim$170 km s$^{-1}$), highest [N II]/H$\alpha$, [S II]/H$\alpha$ and [O I]/H$\alpha$ line ratios, highest velocity residuals from the rotation model, high electron density (>300 cm$^{-3}$) and highest gas temperatures ($\sim$18 000 K). We conclude that this region is tracing a gas outflow in lateral expansion, due to the passage of the radio jet, which is oriented approximately perpendicularly to the nuclear strip. The characteristics of this region all point to shocks being the main mechanism of gas excitation. Photoionization from the AGN radiation seems to dominate along the ionization axis and the jet axis, where we observe increased values of [O III]/H$\beta$ line ratio.

We estimate small values of mass outflow rate and outflow kinetic power, $0.15 < \dot{M}_{out} < 0.17\,M_\odot$ yr$^{-1}$ and $4.7 < \dot{E} < 5.3 \times 10^{39}$ erg s$^{-1}$, respectively. This represents only $2.6 < \dot{E}/L_{bol} < 3.0 \times 10^{-3}$ per cent. These values are comparable to estimates of kinetic power related to warm outflowing gas in other local radio galaxies. However, in order to better understand the properties of the outflow, further observations of molecular gas emission would be necessary.

Although the gas kinematics seems to be dominated by rotation (in the disc) and outflow (along the nuclear strip), we observe a possible signature of gas inflow: increased [O I]/H$\alpha$ values along two spiral arms in the disc, where we also observe an increase in velocity dispersion. We interpret that these arms trace shocks in the rotating gas, which allows a decrease in angular momentum resulting in gas inflow.

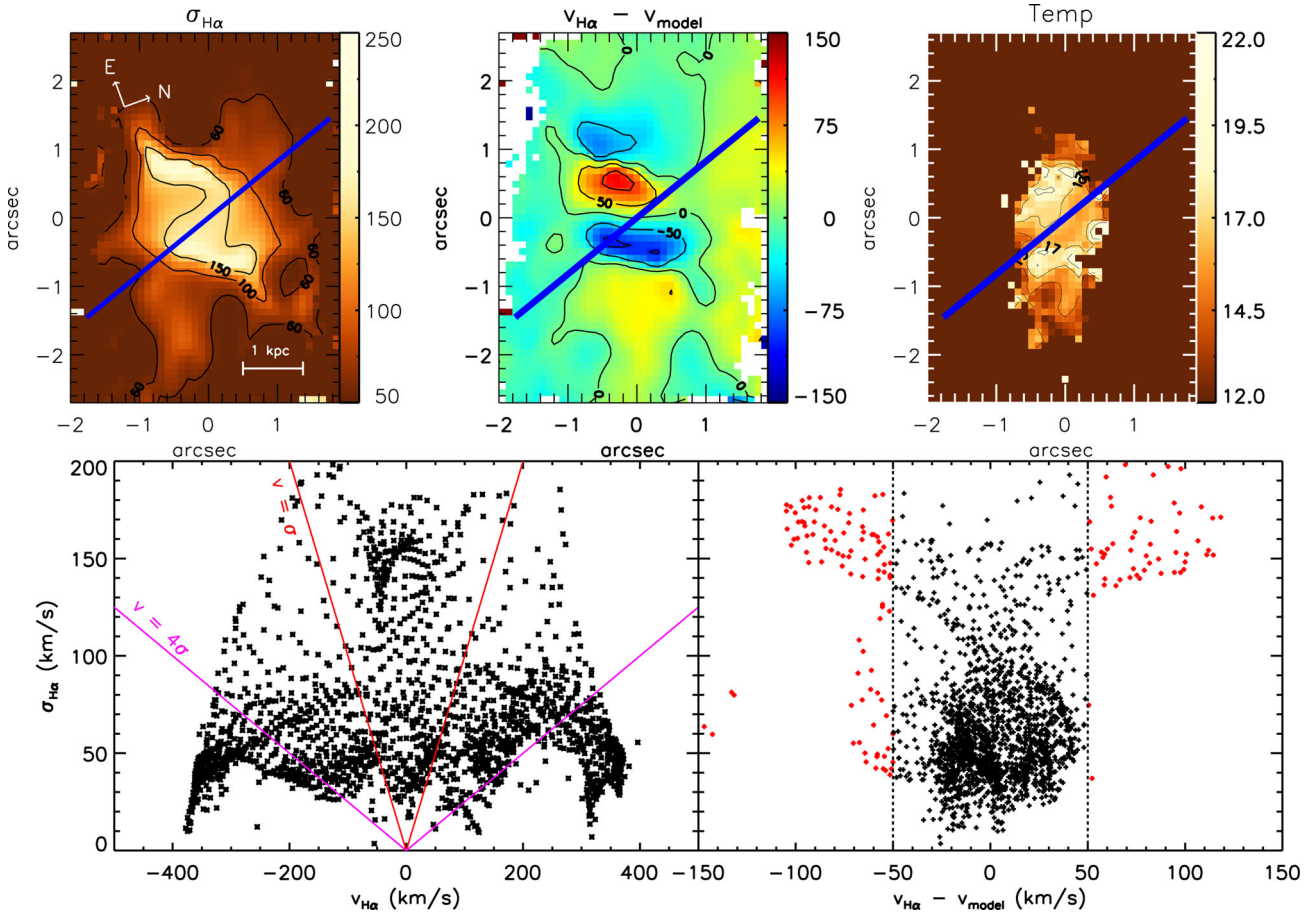


**Figure 13.** Top panels: H$\alpha$ velocity dispersion, rotation model residuals and gas temperatures, as already shown in Figs 4, 12 and 11. The blue line displays the radio jet axis. Velocity and temperature units are km s$^{-1}$ and $\times$ 10$^3$ K, respectively. Bottom panels: diagrams of the relations of the H$\alpha$ velocity dispersion with H$\alpha$ centroid velocity (left) and rotation model residuals (right). Each asterisk represents a pixel of the GMOS FoV. The red and magenta lines in the left diagram represent $v = \sigma$ and $v = 4\sigma$, respectively. The red asterisks in the right diagram represent pixels where the residuals are greater than $\pm$50 km s$^{-1}$, delimited by the dashed line.

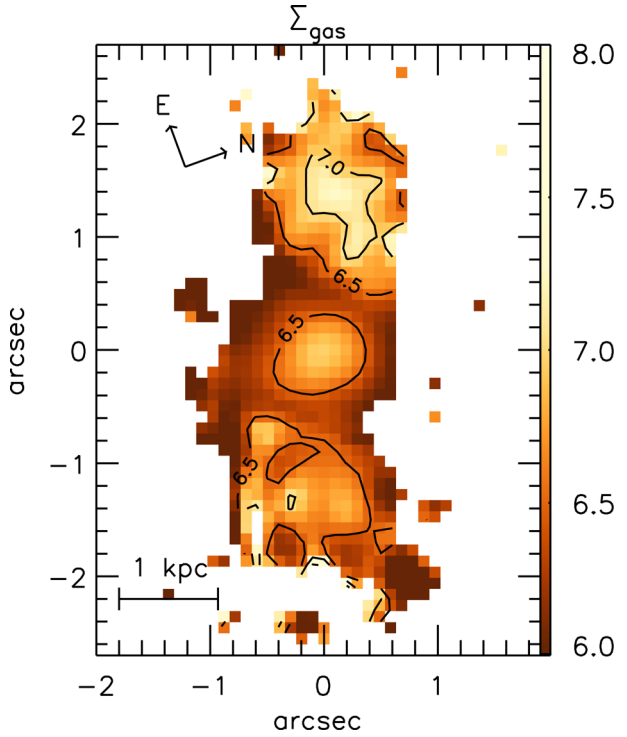


**Figure 14.** Ionized gas mass distribution of 3C 33. Units are $M_\odot$ and are in logarithmic scale. Regions where H$\beta$ were masked out due to high uncertainties were also masked out in this map. However the mass values decrease to negligible values in these regions, and do not affect the total mass estimative.

We have obtained a total mass of ionized gas within the inner $\sim$2.5 kpc of $M = 4.1 \pm 1.7 \times 10^8\,M_\odot$. Its high rotation velocity amplitude ($\sim\pm$ 450 km s$^{-1}$) and the somewhat lower metallicity ($12 + \log(O/H) \sim 8.5-8.8$) than typically observed in the nuclear region of AGNs suggest that this gas has been recently acquired in an interaction event that was probably the trigger of the nuclear activity in 3C33.

## ACKNOWLEDGEMENTS

This work is based on observations obtained at the Gemini Observatory, which is operated by the Association of Universities for Research in Astronomy, Inc., under a cooperative agreement with the NSF on behalf of the Gemini partnership: the National Science Foundation (United States), the National Research Council (Canada), CONICYT (Chile), the Australian Research Council (Australia), Ministério da Ciência, Tecnologia e Inovação (Brazil) and Ministerio de Ciencia, Tecnología e Innovación Productiva (Argentina). This work has been partially supported by the Brazilian institutions CNPq and FAPERGS. Some/all of the data presented in this paper were obtained from the Mikulski Archive for Space Telescopes (MAST). STScI is operated by the Association of Universities for Research in Astronomy, Inc., under NASA contract NAS5-26555. Support for MAST for non-HST data is provided by the NASA Office of Space Science via grant NNX09AF08G and by other grants and contracts.

## REFERENCES

Allen M. G., Groves B. A., Dopita M. A., Sutherland R. S., Kewley L. J., 2008, APJS, 178, 20
Baldwin J. A., Phillips M. M., Terlevich R., 1981, PASP, 93, 5
Bertola F., Bettoni D., Danziger J., Sadler E., Sparke L., de Zeeuw T., 1991, ApJ, 373, 369
Best P. N., Röttgering H. J. A., Longair M. S., 2000, MNRAS, 311, 23
Cardelli J. A., Clayton G. C., Mathis J. S., 1989, ApJ, 345, 245
Couto G. S., Storchi-Bergmann T., Axon D. J., Robinson A., Kharb P., Riffel R. A., 2013, MNRAS, 435, 2982
Couto G. S., Storchi-Bergmann T., Robinson A., Riffel R. A., Kharb P., Lena D., Schnorr-Müller A., 2016, MNRAS, 458, 855
Di Matteo T., Springel V., Hernquist L., 2005, Nature, 433, 604
Fabian A. C., 2012, ARAA, 50, 455
Feruglio C., Maiolino R., Piconcelli E., Menci N., Aussel H., Lamastra A., Fiore F., 2010, A&A, 518, L155
Fragile P. C., Murray S. D., Anninos P., van Breugel W., 2004, ApJ, 604, 74
García-Burillo S. et al, 2014, A&A, 567, A125
Giovannini G., Taylor G. B., Feretti L., Cotton W. D., Lara L., Venturi T., 2005, ApJ, 618, 635
Greene J. E., Ho L. C., 2006, ApJ, 641, 117
Groves B. A., Dopita M. A., Sutherland R. S., 2004, APJS, 153, 9
Heckman T. M., Illingworth G. D., Miley G. K., van Breugel W. J. M., 1985, ApJ, 299, 41
Holt J., Tadhunter C., Morganti R., Bellamy M., González Delgado R. M., Tzioumis A., Inskip K. J., 2006, MNRAS, 370, 1633
Kewley L. J., Groves B., Kauffmann G., Heckman T., 2006, MNRAS, 372, 961
Kormendy J., Ho L. C., 2013, ARAA, 51, 511
Leahy J. P., Perley R. A., 1991, AJ, 102, 537
Luridiana V., Morisset C., Shaw R. A., 2015, A&A, 573, A42
Mahony E. K., Oonk J. B. R., Morganti R., Tadhunter C., Bessiere P., Short P., Emonts B. H. C., Oosterloo T. A., 2016, MNRAS, 455, 2453
Nesvadba N. P. H. et al., 2010, A&A, 521, A65
Osterbrock D. E., Ferland G. J., 2006, Astrophysics of Gaseous Nebulae and Active Galactic Nuclei, 2nd edn. University Science Books, Sausalito, CA
Peterson B. M., 1997, An Introduction to Active Galactic Nuclei. Cambridge Univ. Press, Cambridge
Ramos Almeida C., Tadhunter C. N., Inskip K. J., Morganti R., Holt J., Dicken D., 2011, MNRAS, 410, 1550
Roche N., Humphrey A., Lagos P., Papaderos P., Silva M., Cardoso L. S. M., Gomes J. M., 2016, MNRAS, 459, 4259
Rodríguez-Ardila A., Prieto M. A., Viegas S., Gruenwald R., 2006, ApJ, 653, 1098
Santoro F., Oonk J. B. R., Morganti R., Oosterloo T., 2015, A&A, 574, 89
Simkin S. M., 1979, ApJ, 234, 56
Sofue Y., Tutui Y., Honma M., Tomita A., Takamiya T., Koda J., Takeda Y., 1999, ApJ, 523, 136
Storchi-Bergmann T., Schmitt H. R., Calzetti D., Kinney A. L., 1998, AJ, 115, 909
Tadhunter C., Dicken D., Morganti R., Konyves V., Ysard N., Nesvadba N., Ramos Almeida C., 2014, MNRAS, 445, L51
Tremblay G. R. et al., 2009, APJS, 183, 278
van der Kruit P. C., Allen R. J., 1978, ARAA, 16, 103
Wagner A. Y., Bicknell G. V., 2011, ApJ, 728, 29

This paper has been typeset from a TEX/LATEX file prepared by the author.